Dynamical properties and melting of binary two-dimensional colloidal alloys

I. R. O. Ramos,[1,2] W. P. Ferreira,[1] F. F. Munarin,[3] and F. M. Peeters[1,4]

[1]*Departamento de Física, Universidade Federal do Ceará, Caixa Postal 6030, Campus do Pici, 60455-760 Fortaleza, Ceará, Brazil*

[2]*Universidade Federal Rural do Semi-árido, Campus Pau dos Ferros, Pau dos Ferros, Rio Grande do Norte, Brazil*

[3]*Centro de Tecnologia, Bloco 710, Universidade Federal do Ceará, Campus do Pici, 60455-760 Fortaleza, Ceará, Brazil*

[4]*Department of Physics, University of Antwerp, Groenenborgerlaan 171, B-2020 Antwerpen, Belgium*

(Received 11 March 2013; revised manuscript received 18 September 2014; published 22 December 2014)

A two-dimensional (2D) binary colloidal system consisting of interacting dipoles is investigated using an analytical approach. Within the harmonic approximation we obtain the phonon spectrum of the system as a function of the composition, dipole-moment ratio, and mass ratio between the small and big particles. Through a systematic analysis of the phonon spectra we are able to determine the stability region of the different lattice structures of the colloidal alloys. The gaps in the phonon frequency spectrum, the optical frequencies in the long-wavelength limit, and the sound velocity are discussed as well. Using the modified Lindemann criterion and within the harmonic approximation we estimate the melting temperature of the sublattice generated by the big particles.

DOI: 10.1103/PhysRevE.90.062311 PACS number(s): 82.70.Dd, 64.70.pv, 64.70.D−

I. INTRODUCTION

Colloids are useful model systems not only for important physical phenomena such as crystallization and melting [1,2] but also for solids, especially because of the orders-of-magnitude slower temporal and larger spatial scales that allow the use of videomicroscopy techniques [3,4] and, therefore, properties such as structure, phonons, and melting can be studied in real time [5]. There are several possibilities (e.g., at interfaces, in between glass plates, and patterned substrates) to stabilize the colloidal particles into a reduced dimensional system such as channels and planar substrates. Additionally, the interaction between the colloidal particles and thus the physical properties of the system can be externally controlled, e.g., by means of external magnetic [6] and/or electric fields [7].

Colloidal systems composed of two different types of dipolar particles confined in a monolayer structure have attracted the attention of many theoretical and experimental researchers. Stirner *et al.* [8] performed molecular dynamics simulations at finite temperatures of a binary colloidal monolayer of two different particle sizes at an oil-water interface whose interparticle interaction is governed by an effective dipole potential. The simulations showed that for certain ratios of small (B) to large (A) particles, e.g., 2:1 (AB_2) and 6:1 (AB_6), the system forms a two-dimensional (2D) crystal. In both cases the crystal is composed of a hexagonal lattice of large particles with a unit cell composed of one A particle and two B particles for AB_2 and one A particle and six B particles for AB_6. Studies of the zero-temperature ($T = 0$) phase diagram of a 2D binary system of dipoles using lattice-sum calculations [9] and genetic algorithms [10,11] predicted the formation of several possible lattice structures as a function of the composition and the susceptibility ratio.

The structural behavior of binary mixtures of superparamagnetic colloidal particles at an air-water interface was investigated using integral equation theory together with computer simulations [12,13] and experiments [13,14]. Those studies, however, found only a partial clustering of small particles [12,13] and a local crystalline order [14].

More recently, an interesting experimental and theoretical study [15] of a 2D binary colloidal system of large (A) and small (B) silica particles at an octane-water interface was presented as a function of the relative concentration of small particles $\xi = \rho_B/(\rho_A + \rho_B)$, where ρ_A, ρ_B are the 2D densities of A and B particles, respectively. Due to the experimental setup, the particles were supposed to interact through a repulsive dipole-dipole potential and it was found that the system self-assemblies in a *hexagonal alloy phase* (HAP). Also, it was shown that while the HAP for $\xi = 2/3$ (AB_2) and $\xi = 6/7$ (AB_6) are thermodynamically stable, the HAP for $\xi = 3/4$ (AB_3) and $\xi = 5/6$ (AB_5) was unstable. A comparison between the radial distribution function of the small B particles around the A particles $g_{AB}(r)$ obtained from the analytical MEC with the one obtained from $T \neq 0$ Monte Carlo simulations, which were based on a finite-size computational unit cell, was further used in order to determine if the configuration was stable. The structure and melting behavior of the system was also studied theoretically as a function of the composition and the dipole-moment ratio, using a lattice-sum method and Monte Carlo simulations [16]. By investigating the radial distribution function for small particles $g_{BB}(r)$ as a function of temperature, it was found that the melting temperature of the AB_2 and AB_6 configurations was three orders of magnitude larger than that of the AB_5 structure [16].

In this work, we address the phonon spectrum and melting of a 2D binary colloidal system of dipoles which consists of particles with small and large dipole moments μ_B and μ_A, respectively. Within the *harmonic approximation* we calculate the phonon spectrum of the system for different values of the dipole-moment ratio $s_B = \mu_B/\mu_A$, the relative concentration of small particles ξ, and mass ratio $m^* = m_B/m_A$. The motivation to do so is twofold: (1) it is possible to tune the number and width of the phonon gaps, and the shape of the phonon bands, by changing parameters such as the dipole-moment ratio, composition, and mass ratio [17] and (2) the study of the phonon spectra tells us additionally if the colloidal alloys are stable, i.e., have real phonon frequencies. Specifically, through a systematic analysis of the dispersion relation we determine the interval of values of s_B for which the considered colloidal alloys are stable. Furthermore, the study of the dispersion relation allows us to obtain the sound velocity

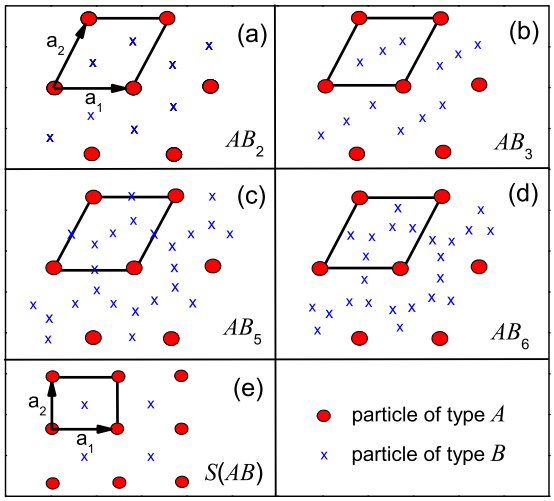

FIG. 1. (Color online) Structures of the colloidal alloys (a) AB_2, (b) AB_3, (c) AB_5, (d) AB_6, and (e) $S(AB)$. The unit cell of each phase is shown by the solid box and the primitive vectors are explicitly shown.

and the optical frequencies in the long-wavelength limit. We also present an estimation of the melting temperature of the sublattice generated by the big particles (type A) as a function of s_B, ξ, and m^* using the modified Lindemann criterion. As a consequence, we found it is possible to specify the optimum value of s_B for which the melting temperature of the system for a given composition is maximum.

In most part of this work, we will concentrate on the perfectly ordered 2D *hexagonal* colloidal alloys in order to model some of the configurations observed experimentally in Ref. [15], namely the configurations for $\xi = 2/3$ (AB_2), $\xi = 3/4$ (AB_3), $\xi = 5/6$ (AB_5), and $\xi = 6/7$ (AB_6). Additionally, we also studied a 2D *square* alloy for $\xi = 1/2$ ($S(AB)$). The lattice structures for these colloidal alloys are illustrated in Fig. 1. It is worth emphasizing that in our calculations we considered crystal structures, i.e., perfect periodic arrangements where defects and boundary effects are absent, in contrast with real experiments where, in general, defects, finite-size effects, or distortions of the crystal structure away from HAP might be present. Thus, although a small number of defects can be considered negligible from an experimental point of view (they may act as a stabilizing factor), they are determinant for the stability of the considered lattice from a theoretical point of view. For example, we find through analytical calculations (harmonic approach) that our perfect hexagonal alloy phase (HAP) for $\xi = 2/3$ (AB_2) is not always stable even for the same set of parameters considered in the experiments [15], which indicates that some distortion with respect to the perfect HAP might be present in order to stabilize the experimentally observed configuration. Indeed, using Monte Carlo simulations (not shown), we find that a slightly distorted crystal structure with respect to the perfect HAP, which is similar to the one previously pointed out in Refs. [11,16], is observed as the ground state for the same value of the dipole-moment ratio ($s_B \approx 0.027$) found analytically.

The paper is organized as follows. In Sec. II, we introduce the model, define the parameters used to characterize the system, and present the colloidal alloys considered in this work. In Sec. III, we present the calculation of the dispersion relation and discuss the numerical results. In Sec. IV, we study the melting behavior of the system. Our conclusions are given in Sec. V.

II. MODEL

We study a 2D binary colloidal system of dipole particles. The particles denoted by A and B have dipole moments μ_A and μ_B, respectively, directed perpendicularly to the plane. The interaction potential is of the dipole-dipole form and can be written in two different ways:

$$U_{kj}(r) = \frac{\mu_k \mu_j}{r^3} \tag{1}$$

or

$$\beta U_{kj}(r) = \Gamma \frac{s_k s_j a^3}{r^3}, \tag{2}$$

where $k, j = A, B$ and

$$\Gamma = \frac{\mu_A^2}{k_B T a^3}, \tag{3}$$

is the dimensionless interaction strength, which relates the potential and the thermal energy, r is the distance between two particles, k_B the Boltzmann constant, T the temperature of the system, a the lattice parameter of the A particles, $\beta = 1/k_B T$, and $s_B = \mu_B/\mu_A$ is the dipole-moment ratio.

For the experimental system studied in Ref. [15], A and B stand for the large and small synthetic amorphous silica particles with diameters 3.00 ± 0.05 μm and 1.00 ± 0.05 μm, respectively, located at an octane-water interface. In this case, the dipoles are mainly due to the residual charges at the particle-oil interface, and the considered dipole-moment ratio was $s_B = 0.037$. On the other hand, for the experimental setup considered in Refs. [13] and [14], A and B represent the large and small superparamagnetic colloidal particles, respectively, at a water-air interface. For instance, from Ref. [13], the big particles have diameter 4.7 μm, mass density $d_A = 1.3$ g/cm^3, and magnetic susceptibility $\chi_A = 6.2\times10^{-11}$ Am^2/T, while the small ones have diameter 2.8 μm, mass density $d_B = 1.5$ g/cm^3, and magnetic susceptibility $\chi_B = 6.6\times10^{-12}$ Am^2/T. An external magnetic field $\vec{B}$ applied perpendicularly to the water-air interface induces in each particle a magnetic moment $\vec{\mu}_i = \chi_i \vec{B}$, where $i = A, B$. Thus, the dipole-moment ratio is $s_B \approx 0.1$.

The colloidal alloy phases depend on the dipole-moment ratio as well as the relative concentration of small particles,

$$\xi = \frac{\rho_B}{\rho_A + \rho_B}, \tag{4}$$

where ρ_A and ρ_B are the 2D densities of A and B particles, respectively.

In the present paper we will study the phonons and melting of (1) perfect 2D *hexagonal* colloidal alloys in order to model the configuration found in Ref. [15]: the hexagonal configurations for $\xi = 2/3 (AB_2)$, $\xi = 3/4$ (AB_3), $\xi = 5/6$ (AB_5), and $\xi = 6/7 (AB_6)$; and (2) a 2D *square* alloy for $\xi = 1/2 (S(AB))$.

The system at hand is 2D with unit cell having one A particle and n small B particles. Therefore, the equilibrium positions of A particles and of n B particles are given by $\vec{R}_A = \vec{R}$, and $\vec{R}_{B_i} = \vec{R} + \vec{c}_i$, where $\vec{R} = l_1\vec{a}_1 + l_2\vec{a}_2$ with l_1, l_2 integers, $\vec{a}_1$, $\vec{a}_2$ are the primitive vectors, $\vec{c}_i = \alpha_i\vec{a}_1 + \beta_i\vec{a}_2$, where $\alpha_i, \beta_i \in (0,1)$ are determined by minimizing the energy for a given dipole-moment ratio, and $i = 1, \ldots, n$. The primitive vectors of the hexagonal lattice are $\vec{a}_1 = a(1,0)$ and $\vec{a}_2 = a(1/2, \sqrt{3}/2)$, while, for the square lattice, $\vec{a}_1 = a(1,0)$ and $\vec{a}_2 = a(0,1)$. Since the colloidal alloys considered here have only one A particle per unit cell, the density of A particles ρ_A is given by $\rho_A a^2 = 2/\sqrt{3}$ and $\rho_A a^2 = 1$ for hexagonal and square unit cells, respectively.

III. PHONON SPECTRUM

The phonon spectrum will be calculated within the harmonic approximation. In this approach, one considers that each particle executes small oscillations (compared to the average distance between the particles) around its equilibrium position and, therefore, one expands the potential energy up to the second order in the deviations from its equilibrium position. Due to the periodicity of the system, one introduces Bloch plane wavelike solutions and thus one obtains (for a given wave vector $\vec{q}$ along the high-symmetry directions of the first Brillouin zone) the dynamical matrix whose eigenvalues and eigenvectors are the square frequencies of vibration, $\omega^2(\vec{q}, j)$, and the direction of vibration, $\vec{e}(\vec{q}, j)$, respectively, with $j = 1, \ldots, 2n_p$, where n_p is the total number of particles per unit cell.

The study of the dispersion relation gives us additionally the stability of the mentioned colloidal alloys, for a given dipole-moment ratio s_B. The considered crystal structure of the colloidal alloy is stable only if $\omega^2(\vec{q}, j) \geqslant 0$ for all $\vec{q}$ and j [18–22]. For $\omega^2(\vec{q}, j) < 0$ the frequencies are imaginary, i.e., the amplitude of particle oscillation becomes an exponentially increasing function of time [22]. It implies that the corresponding crystal structure of the colloidal alloy is unstable and will not exist.

All the colloidal alloys considered in this work have more than one particle per unit cell. As a consequence, there are several acoustical and optical modes which can be associated to in-phase and out-of-phase vibrations of particles in the unit cell, respectively. The acoustical branch is characterized by $\omega(\vec{q}) \to 0$ for $\vec{q} \to 0$, while for the optical branch $\omega(\vec{q}) \to$ const in the limit $\vec{q} \to 0$. Besides, the acoustical and optical branches have a longitudinal, $\vec{e} \parallel \vec{q}$, and a transverse mode, [22] $\vec{e} \perp \vec{q}$.

The dynamical matrix is given by [19,22,23]

$$C_{\alpha\beta}(kk' \mid \vec{q}) = \frac{1}{\sqrt{m_k m_{k'}}} \sum_{l'} \phi_{\alpha\beta}(lk, l'k')\, e^{-i\vec{q}\cdot(\vec{R}_{lk} - \vec{R}_{l'k'})}, \quad (5)$$

where $\phi(r)$ is the interaction potential and

$$\phi_{\alpha\beta}(lk, l'k') = \partial_\alpha \partial_\beta \phi(\vec{R}_{lk} - \vec{R}_{l'k'}) \quad (6)$$

are the force constants with $\alpha, \beta = x, y$. Furthermore, $\vec{R}_{lk} = \vec{R}(l) + \vec{R}(k)$ is the equilibrium position vector of the kth particle in the lth unit cell of the crystal, m_k is its mass, and $\vec{R}(l) = \vec{R}$. Besides, the force constants have the property

$$\sum_{lk, l'k'} \phi_{\alpha\beta}(lk, l'k') = 0, \quad (7)$$

which will be useful in our further calculations. Thus, the equilibrium positions of A particles and of n B particles are given by $\vec{R}_{lA} = \vec{R}_A$ and $\vec{R}_{lB_i} = \vec{R}_{B_i}$. Furthermore, the order of the dynamical matrix is $t = 2n_p \times 2n_p$, i.e., it depends on the considered 2D lattice. The dynamical matrix can be written as

$$D = \begin{pmatrix} D^{AA} & D^{AB_1} & \ldots & D^{AB_n} \\ D^{B_1A} & D^{B_1B_1} & \ldots & D^{B_1B_n} \\ \cdot & \cdot & \cdots & \cdot \\ \cdot & \cdot & \cdots & \cdot \\ \cdot & \cdot & \cdots & \cdot \\ D^{B_nA} & D^{B_nB_1} & \ldots & D^{B_nB_n} \end{pmatrix}, \quad (8)$$

where D^{AA}, $D^{AB_1}, \ldots, D^{B_nB_n}$ are 2×2 block matrices. From Eqs. (5) and (7), the elements of the block D^{AA} are written by

$$D^{AA}_{\alpha\beta}(\vec{q}) = \frac{1}{m_A}\left[S^{AA}_{\alpha\beta}(0) + \sum_i SI1^{AB_i}_{\alpha\beta}(0) - S^{AA}_{\alpha\beta}(\vec{q})\right], \quad (9)$$

where

$$S^{AA}_{\alpha\beta}(\vec{q}) = -\mu_A^2 \lim_{r\to0} \partial_\alpha\partial_\beta \psi_0(\vec{r}, \vec{q}), \quad (10a)$$

$$SI1^{AB_i}_{\alpha\beta}(\vec{q}) = -s_B\mu_A^2 \lim_{r\to0} \partial_\alpha\partial_\beta \psi^i_{I1}(\vec{r}, \vec{q}), \quad (10b)$$

with

$$\psi_0(\vec{r}, \vec{q}) = \sum_{\vec{R}\neq\vec{0}} \frac{e^{-i\vec{q}\cdot\vec{R}}}{|\vec{r} + \vec{R}|^3}, \quad (11a)$$

$$\psi^i_{I1}(\vec{r}, \vec{q}) = \sum_{\vec{R}} \frac{e^{-i\vec{q}\cdot(\vec{R}+\vec{c}_i)}}{|\vec{r} + \vec{R} + \vec{c}_i|^3}. \quad (11b)$$

On the other hand, from Eq. (5) we found

$$D^{AB_i}_{\alpha\beta}(\vec{q}) = \frac{1}{\sqrt{m_A m_B}}\left[-SI1^{AB_i}_{\alpha\beta}(\vec{q})\right]. \quad (12)$$

In the same spirit of Refs. [18–20], we used the Ewald summation technique and transformed Eqs. (11a) and (11b) into expressions which converge rapidly. Thus, we obtain [20]

$$\psi_0(\vec{r}, \vec{q}) = \pi\rho_A \sum_{\vec{G}} e^{i(\vec{q}+\vec{G})\cdot\vec{r}} \Upsilon\left(\frac{|\vec{q} + \vec{G}|}{2\varepsilon}, 0\right) + \frac{2\varepsilon e^{-\varepsilon^2 r^2}}{\sqrt{\pi} r^2} - \frac{\mathrm{erf}(\varepsilon r)}{r^3} + \sum_{\vec{R}\neq\vec{0}} e^{-i\vec{q}\cdot\vec{R}} \Omega_1(|\vec{r} + \vec{R}|), \quad (13)$$

with

$$\Upsilon\left(\frac{|\vec{q} + \vec{G}|}{2\varepsilon}, 0\right) = \frac{4\varepsilon}{\sqrt{\pi}} e^{-|\vec{q}+\vec{G}|^2/4\varepsilon^2} - 2|\vec{q} + \vec{G}|\,\mathrm{erfc}\left(\frac{|\vec{q} + \vec{G}|}{2\varepsilon}\right) \quad (14a)$$

and

$$\Omega_1(x) = \frac{\mathrm{erfc}(\varepsilon x)}{x^3} + \frac{2\varepsilon}{\sqrt{\pi}} \frac{e^{-\varepsilon^2 x^2}}{x^2} \quad (14b)$$

where the parameter $\varepsilon > 0$ is related to the density of large particles, i.e., $\varepsilon = \sqrt{\pi\rho_A}$. Besides, we have

$$\psi^i_{I1}(\vec{r},\vec{q}) = \pi\rho_A \sum_{\vec{G}} e^{i(\vec{q}+\vec{G})\cdot\vec{r}} e^{i\vec{G}\cdot\vec{c}_i} \Upsilon\left(\frac{|\vec{q}+\vec{G}|}{2\varepsilon},0\right) + \sum_{\vec{R}} e^{-i\vec{q}\cdot(\vec{R}+\vec{c}_i)} \Omega_1(|\vec{r}+\vec{R}+\vec{c}_i|) \quad (15)$$

and, therefore, the block matrices D^{AA} and D^{AB_i} involve only rapidly convergent sums. On the other hand, the block $D^{B_iB_j}$, $i \neq j$, and $D^{B_iB_i}$ are written as

$$D^{B_iB_j}_{\alpha\beta}(\vec{q}) = \frac{1}{m_B}\left[-SII1^{B_iB_j}_{\alpha\beta}(\vec{q})\right], \quad (16a)$$

$$D^{B_iB_i}_{\alpha\beta}(\vec{q}) = \frac{1}{m_B}\left[s_B^2 S^{AA}_{\alpha\beta}(0) + \sum_{j\neq i} SII1^{B_iB_j}_{\alpha\beta}(0) + SI1^{AB_i}_{\alpha\beta}(0) - s_B^2 S^{AA}_{\alpha\beta}(\vec{q})\right], \quad (16b)$$

with

$$SII1^{B_iB_j}_{\alpha\beta}(\vec{q}) = -s_B^2\mu_A^2 \lim_{r\to 0} \partial_\alpha\partial_\beta \psi^{ij}_{II1}(\vec{r},\vec{q}), \quad (17a)$$

$$\psi^{ij}_{II1}(\vec{r},\vec{q}) = \sum_{\vec{R}} \frac{e^{-i\vec{q}\cdot(\vec{R}+\vec{c}_{ij})}}{|\vec{r}+\vec{R}+\vec{c}_{ij}|^3} \quad (17b)$$

$$\vec{c}_{ij} = \vec{c}_i - \vec{c}_j. \quad (17c)$$

Again, the expression for $\psi^{ij}_{II1}(\vec{r},\vec{q})$ using the Ewald method is given by

$$\psi^{ij}_{II1}(\vec{r},\vec{q}) = \pi\rho_A \sum_{\vec{G}} e^{i(\vec{q}+\vec{G})\cdot\vec{r}} e^{i\vec{G}\cdot\vec{c}_{ij}} \Upsilon\left(\frac{|\vec{q}+\vec{G}|}{2\varepsilon},0\right) + \sum_{\vec{R}} e^{-i\vec{q}\cdot(\vec{R}+\vec{c}_{ij})} \Omega_1(|\vec{r}+\vec{R}+\vec{c}_{ij}|). \quad (18)$$

Since the dynamical matrix is Hermitian, we have $D^{B_iA} = [D^{AB_i}]^\dagger$ and $D^{B_jB_i} = [D^{B_iB_j}]^\dagger$. Because the dynamical matrix involves the mass of the particles, we introduced the parameter $m^* = m_B/m_A$. For Brownian systems one can consider $m^* = 1$, i.e., the particles have the same mass, since the inertial asymmetry between the colloids becomes irrelevant in the overdampped regime [6,17,24]. On the other hand, assuming that the dipole moment of each particle is $\mu_i = \lambda D_i^3$, where λ is a constant of proportionality and D_i is the radius of the particle [10], and that the particles have the same mass density, we obtain $m^* = s_B = \mu_B/\mu_A$. The case with different masses is available experimentally in systems of colloids between glass plates with no solvent [25]. In what follows, we will restrict ourselves to the two cases $m^* = s_B$ and $m^* = 1$.

Figures 2 and 3 show the square of the phonon frequencies in units of $\omega_0^2 = \mu_A^2\rho_A^{5/2}/m_A$ of the structure AB_2 [Fig. 1(a)] for $s_B = 0.015$ and $s_B = 0.037$, considering $m^* = s_B$ and $m^* = 1$, respectively. The square frequencies are shown along the high-symmetry directions in reciprocal space, where the high-symmetry points are shown as insets. For $s_B = 0.015$,

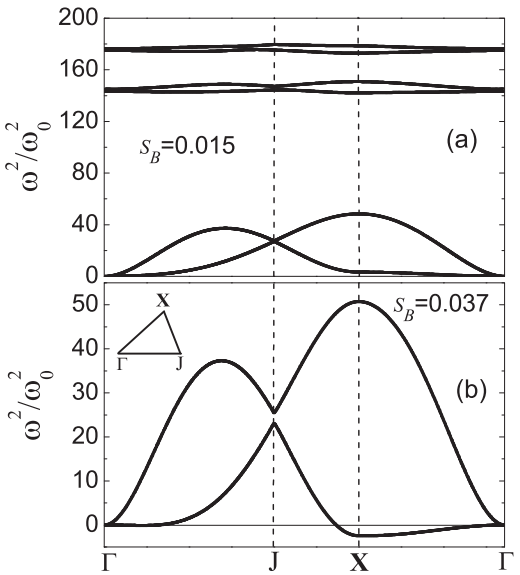

FIG. 2. Square of the phonon frequencies of the crystal phase AB_2 for $m^* = s_B$ in units of $\omega_0^2 = \mu_A^2\rho_A^{5/2}/m_A$ (a) for $s_B = 0.015$ and (b) $s_B = 0.037$, along the high-symmetry directions in reciprocal space. The high-symmetry points Γ, J, and X are shown in the inset of (b). Only the lowest energy modes are shown in (b) in order to enlarge the region around zero frequency.

we found $\omega^2(\vec{q},j) \geqslant 0$ for all the eigenvalues, indicating a stable long-range AB_2 ordered structure. On the other hand, for the dipole-moment ratio $s_B = 0.037$ considered in the experiments performed by Law *et al.* [15], we found $\omega^2(\vec{q},j) < 0$ for some eigenvalues, indicating that the perfect hexagonal AB_2 structure is not stable for $s_B = 0.037$. Actually, we found that on the basis of the requirement of real phonon frequencies, the range of stability for the phase AB_2 is $0 \leqslant s_B \leqslant 0.0269$. We stress that in our calculations the considered perfect

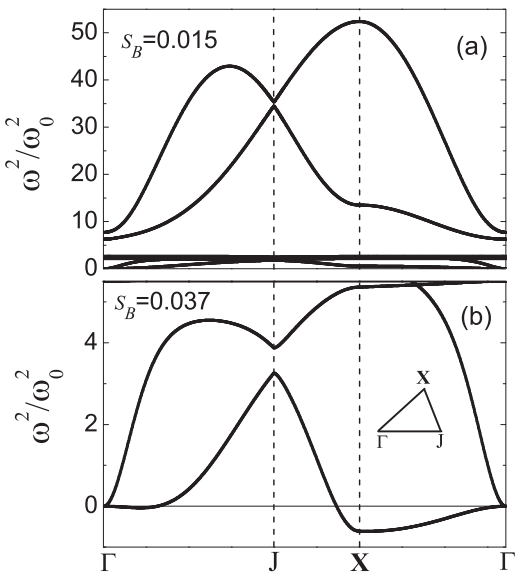

FIG. 3. Square of the phonon frequencies of the phase AB_2 for $m^* = 1$ (a) for $s_B = 0.015$ and (b) $s_B = 0.037$. Only the lowest energy modes are shown in (b).

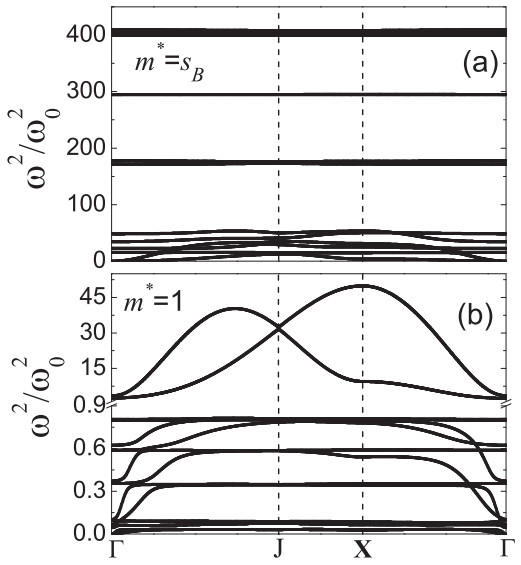

FIG. 4. Square of the phonon frequencies of the phase AB_6 for $s_B = 0.002$ in units of $\omega_0^2 = \mu_A^2 \rho_A^{5/2}/m_A$ for (a) $m^* = s_B$ and (b) $m^* = 1$.

periodic structures are free of defects and boundary effects, in contrast with the situation in real experiment where, in general, defects and imperfections might be present. Thus, although a small number of defects in the configuration AB_2 for $s_B = 0.037$ can be considered negligible from an experimental point of view, they can be determinative for the stability from a theoretical point of view. Our results indicate that the stable phase observed experimentally in Ref. [15] must present some distortion from the perfect hexagonal alloy phase. As a consequence, we did not find long-range order

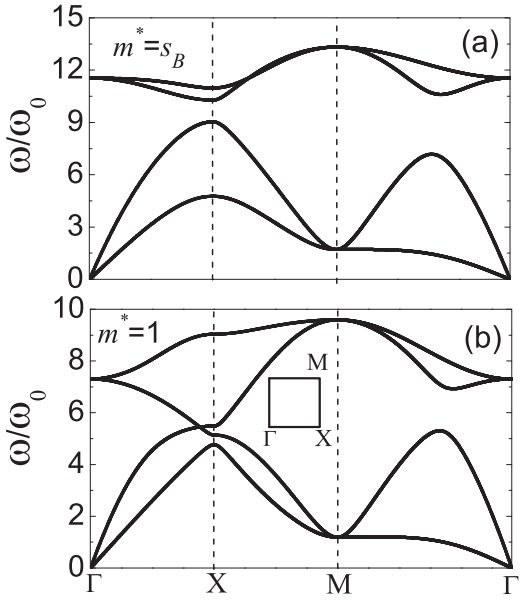

FIG. 5. Dispersion relation of the phase $S(AB)$ for $s_B = 0.25$ along the high-symmetry directions in reciprocal space (a) for $m^* = s_B$ and (b) for $m^* = 1$. The high-symmetry points Γ, X, and M are shown in the inset of (b).

TABLE I. Interval of stability of some colloidal alloys. The phases AB_3 and AB_5 are unstable and therefore are not listed.

Phases	AB_2	AB_6	$S(AB)$
Stable	$0 \leqslant s_B \leqslant 0.0269$	$0 \leqslant s_B \leqslant 0.0043$	$0.038 \leqslant s_B \leqslant 0.29$

for the perfect HAP AB_2 for $s_B = 0.037$, but we found it for $s_B = 0.0269$, which is a slightly lower value. Indeed, we performed Monte Carlo simulations for the specific phase AB_2 (not shown) and found that a slightly distorted crystal structure with respect to the perfect HAP which is also similar to the one previously pointed out in Refs. [11,16] is observed as the ground state for the same value of the dipole-moment ratio ($s_B \approx 0.027$) found analytically.

The presence of gaps in the phonon frequency spectrum is another important characteristic of the structure AB_2. No vibrations are possible for frequencies within the gap. The phonon gaps of the phase AB_2 for $m^* = s_B$, i.e., when the particles have different masses, are larger than the ones for $m^* = 1$. Furthermore, for $m^* = s_B$, the phonon gaps occur between acoustical and optical modes as well as between some of the optical modes, while for $m^* = 1$ the phonon gaps appear only between the optical modes. The thick line in Fig. 3 is due to two optical branches very close to each other that are not distinguishable on the scale used in the figure.

For the structures AB_3 and AB_5 shown in Figs. 1(b) and 1(c), respectively, we found that they are unstable for any dipole-moment ratio, since imaginary phonon frequencies are found. In other words, long-range order is not possible for the configurations AB_3 and AB_5 independently of the value of the dipole-moment ratio. Since in the harmonic approximation, the particles execute only small vibrations around their equilibrium positions, one cannot state that the structures AB_3 and AB_5 are stable at $T = 0$. Our result clearly shows that calculations of the energy of a given lattice structure, even after minimization with respect to some parameters, at $T = 0$, do not guarantee that the obtained MECs are stable.

In Fig. 4 we present the square of the phonon frequencies of the phase AB_6 for $s_B = 0.002$. For the AB_6 configuration, we found that the interval of stability is $0 \leqslant s_B \leqslant 0.0043$.

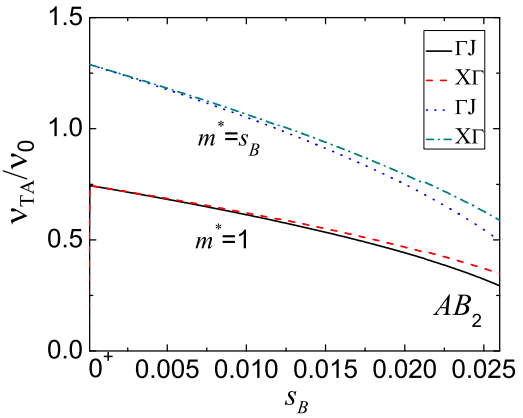

FIG. 6. (Color online) The sound velocity in units of $v_0 = \omega_0/\sqrt{\rho_A}$ of the transverse acoustical mode of the phase AB_2 as a function of s_B for $m^* = 1$ and $m^* = s_B$.

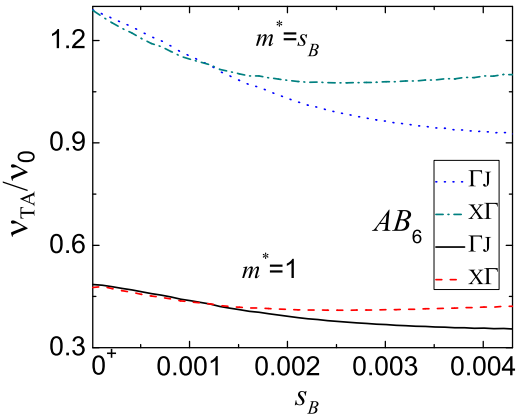

FIG. 7. (Color online) The sound velocity in units of $v_0 = \omega_0/\sqrt{\rho_A}$ of the transverse acoustical mode of the phase AB_6 as a function of s_B for $m^* = 1$ and $m^* = s_B$.

Therefore, if we considered not only the large A particles, there is no long-range AB_6 order for $s_B = 0.037$ which is consistent with the experiments reported in Ref. [15]. However, the most important result for the AB_6 configuration is the considerable increase of the phonon gaps between the optical modes when the particles have different masses. As a consequence, there is a large number of frequencies for which the AB_6 structure cannot sustain vibrations. On the other hand, when the particles have the same mass, only a small phonon gap is found, between the optical modes, similarly to the phase AB_2.

Figure 5 shows the dispersion relation of the configuration $S(AB)$ for $s_B = 0.25$. Again, on the basis of the requirement of real phonon frequencies, we found that the interval of stability of the alloy $S(AB)$ is $0.038 \leqslant s_B \leqslant 0.29$. Interestingly, in this case, we do not have stability for $s_B = 0$, i.e., when only one particle is present in the unit cell. It is well known that a 2D system of particles interacting through a Coulomb potential when arranged in a square Bravais lattice is unstable [18]. Here, the same conclusion is reached when the particles interact through a repulsive dipole-dipole potential. Unlike the phases AB_2 and AB_6 that have phonon gaps for $m^* = s_B$ and $m^* = 1$,

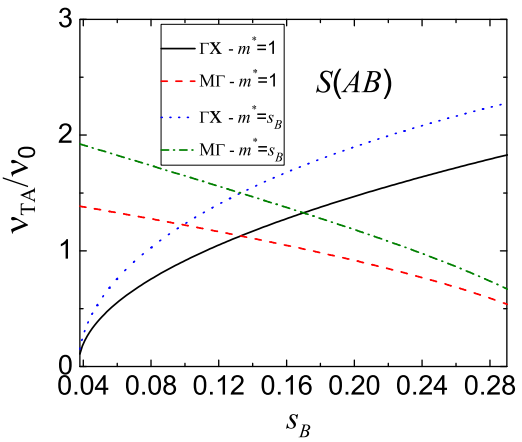

FIG. 8. (Color online) The sound velocity in units of $v_0 = \omega_0/\sqrt{\rho_A}$ of the transverse acoustical mode of the $S(AB)$ as a function of s_B for $m^* = 1$ and $m^* = s_B$.

TABLE II. Fitting parameters [Eq. (19)] for the sound velocity of the phase AB_2.

AB_2	$m^* = s_B$	$m^* = s_B$	$m^* = 1$	$m^* = 1$
Direction	ΓJ	$X\Gamma$	ΓJ	$X\Gamma$
v_0	1.289	1.289	0.744	0.743
v_1	−17.38	−18.32	−9.166	−9.745
v_2	−473.1	−314.4	−294.8	−200.0

the configuration $S(AB)$ exhibits gaps in the phonon spectrum only for $m^* = s_B$. This is an example of how the properties of the system depend on the composition ξ. The interval of stability of some of the colloidal alloys are reported in Table I.

The sound velocity of the transverse acoustical (TA) mode, $v_{TA} = d\omega_{TA}/dq|_{q\to 0}$, is shown for the stable configurations AB_2, AB_6, and $S(AB)$, in Figs. 6, 7, and 8, respectively, along the directions (1,0) and (1,1) (in what follows, the symbol 0^+ means that we are not considering $s_B = 0$ but only s_B values very close to zero). For these phases, the sound velocity is large in the case the particles have different masses. For the structure AB_2, in both directions, we found that the sound velocity decreases with increasing s_B. However, the sound velocity along the direction ΓJ decreases faster than in the direction $X\Gamma$. On the other hand, for the configuration AB_6 we have a different behavior for the sound velocity. In the direction ΓJ, the sound velocity decreases monotonically with increasing s_B, while along the direction $X\Gamma$ the sound velocity decreases up to $s_B = 0.00251$, where the minimum sound velocities $v_{TA}/v_0 = 1.07608$ and $v_{TA}/v_0 = 0.40973$ are observed for $m^* = s_B$ and $m^* = 1$, respectively.

For the configuration $S(AB)$, the s_B dependence of the sound velocity differs completely from the one found for the phases AB_2 and AB_6 as shown in Fig. 8. In the direction ΓX, the velocity increases monotonically with increasing s_B, while the opposite behavior is found along the direction $M\Gamma$. We were able to fit the sound velocity of the phases AB_2, AB_6, and $S(AB)$ to the expression

$$v_{TA}/v_0 = v_0 + v_1 s_B + v_2 s_B^2, \tag{19}$$

where the coefficients v_i are reported in Tables II, III, and IV, respectively.

In Figs. 9(a), 10, and 11 the s_B dependence of the optical frequencies $\omega_{\rm op}$ at the Γ point is presented for both cases $m^* = s_B$ and $m^* = 1$. The optical frequencies are associated with the out-of-phase vibrations of the particles in the unit cell. In general, the number of optical frequencies $n_{\rm op}$ depends on the number of particles per unit cell n_p and the dimensionality of the system, being $n_{\rm op} = 2n_p - 2$ for the 2D colloidal system

TABLE III. Fitting parameters [Eq. (19)] for the sound velocity of the phase AB_6.

AB_6	$m^* = s_B$	$m^* = s_B$	$m^* = 1$	$m^* = 1$
Direction	ΓJ	$X\Gamma$	ΓJ	$X\Gamma$
v_0	1.289	1.288	0.485	0.476
v_1	−176.7	−142.9	−65.16	−50.90
v_2	20861.2	24930.7	7759.54	9060.95

TABLE IV. Fitting parameters [Eq. (19)] for the sound velocity of the phase $S(AB)$.

$S(AB)$	$m^* = s_B$	$m^* = s_B$	$m^* = 1$	$m^* = 1$
Direction	ΓX	$M\Gamma$	ΓX	$M\Gamma$
v_0	0.001	2.015	−0.021	1.417
v_1	13.64	−2.985	10.22	−1.236
v_2	−20.02	−5.899	−13.25	−6.354

at hand. As a general behavior, the optical frequencies for $m^* = s_B$ are larger than those for $m^* = 1$.

The phase AB_2 has 4 optical frequencies and the phase AB_6 has 12, since these alloys have three and seven particles per unit cell, respectively. For the colloidal alloys AB_2 and AB_6, the different optical frequencies are nondegenerate. The jumps of the optical frequencies for the phase AB_2 in Fig. 9(a) are associated with the change of the positions of the small particles in the unit cell as a function of s_B, as can be seen in Fig. 9(b). On the other hand, a different behavior is found for the structure $S(AB)$. In this case, the two allowed optical phonon frequencies are degenerate, which is a consequence of the symmetry of the square lattice structure presented by that phase. The vibrations of the particles in the unit cell are equivalent in both directions.

To conclude, notice that the optical frequencies tend to zero when s_B approaches zero only in the case $m^* = 1$. In this limit ($s_B \to 0$) the interaction involving the small particles B becomes negligible, allowing the optical modes to be excited with a very low frequency.

IV. MELTING

Now we turn our discussion to the melting behavior of the system as a function of the dipole-moment ratio s_B. The melting temperature will be calculated within the harmonic

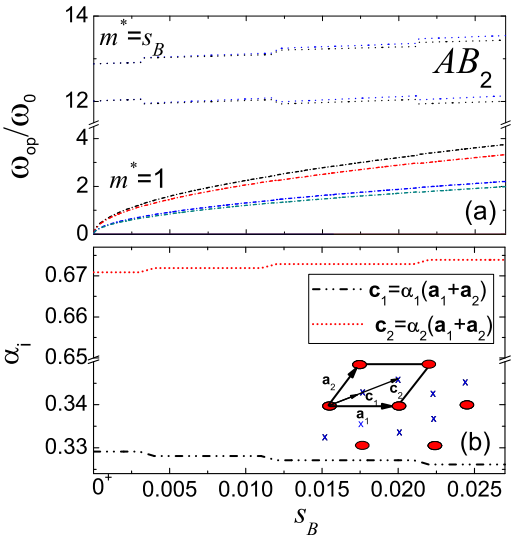

FIG. 9. (Color online) (a) The optical frequencies in units of ω_0 at the Γ point for AB_2 as a function of s_B for $m^* = s_B$ (dotted line) and $m^* = 1$ (short dash dotted line) and (b) positions of the small particles inside the unit cell of the structure AB_2 as a function of s_B.

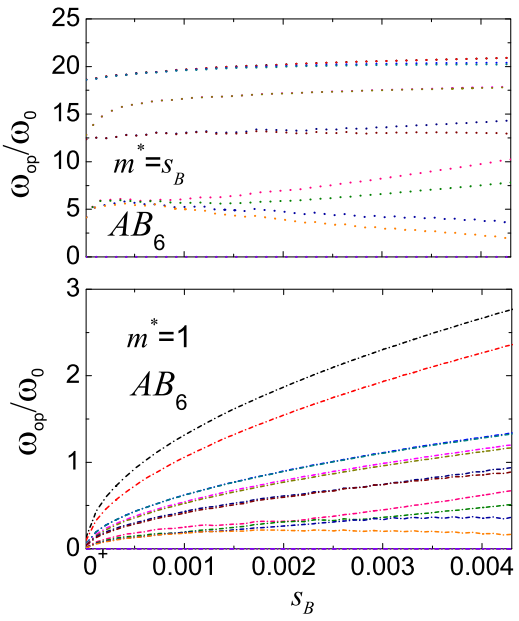

FIG. 10. (Color online) The optical frequencies in units of ω_0 at the Γ point for AB_6 as a function of s_B for $m^* = s_B$ and $m^* = 1$.

approximation using a Lindemann-like criterion. The original Lindemann criterion [26] states that the melting of a given structural phase occurs when the mean-square displacement exceeds a threshold value of the mean interparticle distance r_0 [26–28]:

$$\frac{\langle u^2 \rangle}{r_0^2} = \delta^2, \tag{20}$$

where the parameter δ^2 is obtained numerically from, e.g., molecular dynamics simulation. The symbol $\langle\rangle$ stands for a thermal average. The original Lindemann criterion is not applicable for 2D crystals because $\langle u^2 \rangle$ diverges logarithmically with the size of the system [19,28]. Bedanov *et al.* [28] showed through molecular dynamics simulations that the relative mean-square displacement, given by

$$\langle |\vec{u}(\vec{R}) - \vec{u}(\vec{R} + \vec{a})|^2 \rangle, \tag{21}$$

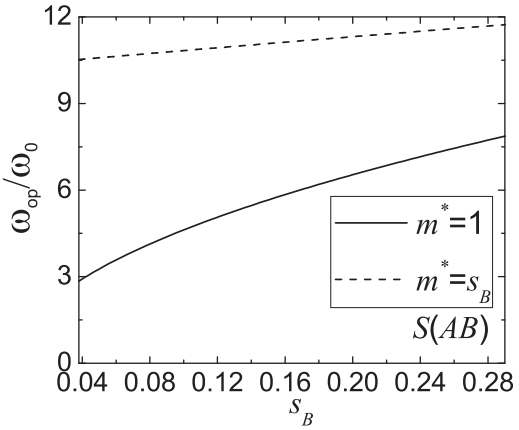

FIG. 11. The optical frequencies in units of ω_0 at the Γ point for $S(AB)$ as a function of s_B for $m^* = s_B$ and $m^* = 1$.

is a well-defined quantity for a 2D infinite system, where $\vec{u}(\vec{R})$ and $\vec{u}(\vec{R}+\vec{a})$ are the displacement vectors at site $\vec{R}$ and at its nearest-neighbor site $\vec{R}+\vec{a}$, respectively, and $\vec{a}$ is the lattice parameter. In Ref. [28], the modified Lindemann-like criterion for 2D crystals was defined as

$$\frac{\langle|\vec{u}(\vec{R})-\vec{u}(\vec{R}+\vec{a})|^2\rangle}{r_0^2}=\delta_m^2, \tag{22}$$

with the modified Lindemann parameter (δ_m^2) typically $\delta_m^2\approx 0.1$. The melting of the B sub-lattice was studied in Ref. [16] using Monte Carlo simulations and the radial distribution function $g_{BB}(r)$ between the small particles was obtained. For instance, the calculated melting temperature of the B sublattice for the AB_2 configuration was $4.0\pm 0.5\times 10^{-3}$ for $s_B=0.025$.

Here we will study the melting behavior of the large A particles. In this case, r_0 in Eq. (22) is the mean interparticle distance between large particles which is related to the density as $r_0=1/\sqrt{\pi\rho_A}$. The parameter δ_m^2 for 2D dipole interaction [28] is $\delta_m^2=0.12$, and, therefore, we will take this value in order to determine the melting temperature (T_M) of the A particles. As shown recently, the B sublattice (small particles) is already melted at T_M, since the melting temperature of the A sublattice (large particles) was estimated to be two orders of magnitude larger than the one for the small particles [16]. In addition, the melting temperature calculated through the harmonic approximation depends on the frequencies of the phonon spectrum which are obtained at $T=0$ by considering both sublattices ordered [e.g., see Eq. (30)]. In the present colloidal alloys the distribution of the small B particles around the big A particles is symmetric. We argue here that since in the melted state the small particles are spread uniformly around the large particles, the effective interaction between small and large particles is very similar to the one found in the crystal structure at $T=0$. In this case, the frequencies of the phonon spectrum obtained at $T=0$ for the ordered arrangement of the colloidal alloy would also in some sense reflect the effective interaction between both types of particles at $T\neq 0$. Therefore, in spite of the B sublattice be already melted at the melting temperature of the A sublattice, we consider the phonon frequencies obtained for the complete ordered structure at $T=0$. We stress that the melting temperature of the large A particles obtained here is only an estimate but we expect that the qualitative trends and the order of magnitude to be correct.

The correlation function $\langle|\vec{u}(\vec{R})-\vec{u}(\vec{R}+\vec{a})|^2\rangle$ is obtained within the harmonic approximation and by considering only the nearest neighbors. In general, each lattice site in the 2D colloidal alloys has several types of nearest neighbors, and the number and the distance of the nearest neighbors depend on the considered colloidal alloy. The melting behavior of the A sublattice will be studied as a function of the dipole-moment ratio s_B for the case $m^*=1$, i.e., when both types of particles have the same mass [17,29] and for $m^*=s_B$.

The correlation function between A particles is given by [19,20]

$$\Delta u_{AA}=\frac{1}{N_A}\sum_{\alpha=x,y}\sum_{l=1}^{N_A}\left\langle\left|u_\alpha^A(0)-u_\alpha^A(l)\right|^2\right\rangle, \tag{23}$$

where $u_\alpha^A(l)$ is the αth component of the displacement vector of the lth nearest neighbor of type A and N_A is the number of nearest neighbors of type A. For the stable configurations AB_2 and AB_6 the A particles are ordered in a hexagonal lattice and therefore each of them has six nearest neighbors. On the other hand, for the phase $S(AB)$ the A particles form a square lattice with each particle having four nearest neighbors.

Using the normal coordinates transformation [20,23],

$$u_\alpha^A(0)=\frac{1}{\sqrt{Nm_A}}\sum_{\vec{q},j}e_\alpha^A(\vec{q},j)Q(\vec{q},j), \tag{24a}$$

$$u_\alpha^A(l)=\frac{1}{\sqrt{Nm_A}}\sum_{\vec{q},j}e_\alpha^A(\vec{q},j)Q(\vec{q},j)e^{i\vec{q}\cdot\vec{R}_A(l)}, \tag{24b}$$

where m_A is the mass of the large particle, N the number of unit cells of the crystal, $e_\alpha^A(\vec{q},j)$ the αth component of the eigenvector of the jth normal mode of the large particle for the wave vector $\vec{q}$, $Q(\vec{q},j)$ the normal coordinate of the vibrational mode, and $\vec{R}_A(l)$ the relative vector connecting one A particle at the origin to its lth nearest neighbor of type A. From the fact that the thermal average of $Q(\vec{q},j)Q^*(\vec{q}',j')$ is given by [20,23]

$$\langle Q(\vec{q},j)Q^*(\vec{q}',j')\rangle=\frac{k_BT}{\omega^2(\vec{q},j)}\delta_{\vec{q}\vec{q}'}\delta_{jj'}, \tag{25}$$

where k_B is the Boltzmann constant and T is the temperature of the system, we obtain

$$\left\langle\left|u_\alpha^A(0)-u_\alpha^A(l)\right|^2\right\rangle=\frac{4k_BT}{Nm_A}\sum_{\vec{q},j}\frac{\left[e_\alpha^A(\vec{q},j)\right]^2}{\omega^2(\vec{q},j)}\sin^2\frac{\vec{q}\cdot\vec{R}_A(l)}{2}. \tag{26}$$

Therefore, the expression for Δu_{AA} results in

$$\Delta u_{AA}=\frac{4k_BT}{Nm_AN_A}\Gamma_{AA}, \tag{27}$$

with

$$\Gamma_{AA}=\sum_{\vec{q},j}\frac{\left[e_x^A(\vec{q},j)\right]^2+\left[e_y^A(\vec{q},j)\right]^2}{\omega^2(\vec{q},j)}\sum_{l=1}^{N_A}\sin^2\frac{\vec{q}\cdot\vec{R}_A(l)}{2}. \tag{28}$$

Now the correlation function becomes

$$\langle|\vec{u}(\vec{R})-\vec{u}(\vec{R}+\vec{a})|^2\rangle=\Delta u_{AA}, \tag{29}$$

and substituting this into the modified Lindemann criterion, we found

$$\Gamma_M=\frac{4\pi}{NN_A\delta_m^2\rho_A^{3/2}a^3}\sum_{\vec{q},j}\frac{\left[e_x^A(\vec{q},j)\right]^2+\left[e_y^A(\vec{q},j)\right]^2}{\omega^2(\vec{q},j)/\omega_0^2}\times\sum_{l=1}^{N_A}\sin^2\frac{\vec{q}\cdot\vec{R}_A(l)}{2}, \tag{30}$$

where $\omega_0^2=\mu_A^2\rho_A^{5/2}/m_A$.

The melting temperature of dipolar systems is usually studied in terms of the dimensionless coupling parameter $\Gamma_M=\mu_A^2/k_BT_Ma^3$, which involves the potential and thermal energy. Here we will plot $1/\Gamma_M$ as a function of the dipole-moment ratio s_B.

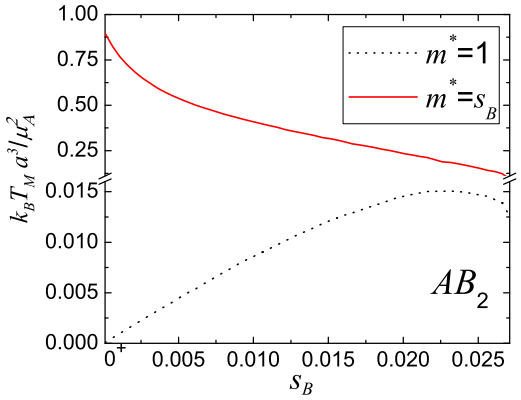

FIG. 12. (Color online) Melting temperature of the A sublattice of the phase AB_2 as a function of the dipole-moment ratio. $m^*=1$ ($m^*=s_B$) means particles A and B with equal (different) masses. For $m^*=1$, the melting temperature assumes the maximum value $1/\Gamma_M=0.01507$ for $s_B=0.0231$.

In Fig. 12 we present the melting behavior of the structure AB_2 ($\xi=2/3$) as a function of the dipole-moment ratio s_B for the cases with equal ($m^*=1$) and different ($m^*=s_B$) masses. As commented before, the symbol 0^+ (in the x axis of Fig. 12) means that we are not considering $s_B=0$ but only s_B values very close to zero. Initially, we will focus on the case with $m^*=1$. For $s_B=0$, i.e., a one-component dipolar system, we found $1/\Gamma_M\approx 0.15$, which is very close to the value $1/\Gamma_M\approx 0.11$ found in Refs. [16] and [30]. Besides, as an important finding, there is an optimum value of the dipole-moment ratio s_B for which the melting temperature of the A sublattice reaches a maximum, i.e., for $s_B=0.0231$ the melting temperature has the maximum value $1/\Gamma_M=0.01507$. This is interesting since it can be used in future experimental studies of 2D binary colloidal systems of dipoles when one wants to maximize the melting temperature. For $s_B=0.025$, which is experimentally relevant [15,16], we find that $1/\Gamma_M=1.45\times10^{-2}$. It means that, for $s_B=0.025$, the melting point of the A sublattice is one order of magnitude larger than that of the B sublattice ($1/\Gamma_M=4.0\pm0.5\times10^{-3}$) calculated using Monte Carlo simulations [16].

In the case of particles having different masses ($m^*=s_B$), we observe a very different qualitative behavior of the melting temperature as a function of s_B. The melting temperature decreases monotonically as s_B is increased. Quantitatively, the melting temperature is more than one order of magnitude larger than for the case with equal masses $m^*=1$. The presence of the lighter small dipoles makes the crystalline structure more stable against thermal fluctuations, as compared to the case with $m^*=1$.

The melting temperature for the phase AB_6 ($\xi=6/7$) as a function of s_B is presented in Fig. 13 for the cases $m^*=1$ and $m^*=s_B$. The same general qualitative behavior found for the phase AB_2 is also observed for the phase AB_6, namely the melting temperature for $m^*=1$ exhibits a maximum but now for a smaller $s_B=0.0033$, while for the case $m^*=s_B$ we observe that the melting temperature decreases with increasing s_B. Also, the melting temperature for $m^*=s_B$ is about two orders of magnitude larger than that for $m^*=1$.

Differently from the smooth behavior found for the phase AB_2, we observe that for the phase AB_6 there are fluctuations in the melting temperature curve as a function of s_B (Fig. 13) due to numerical inaccuracies. The latter is related to the larger number of particles in the unit cell of the phase AB_6 [Fig. 1(d)], which increases the number of phonon modes considerably. As is apparent from Fig. 10 there are many low-frequency modes which are more difficult to calculate numerically with high accuracy. And those frequency modes are the ones that contribute strongly to the melting temperature.

The melting of the A sublattice for the structure $S(AB)$ as a function of s_B, for $m^*=1$ and $m^*=s_B$, is presented in Fig. 14. Unlike the configurations AB_2 and AB_6, the phase $S(AB)$ has the same qualitative behavior for $m^*=1$ and $m^*=s_B$. On the other hand, quantitatively, the maximum melting temperature for $m^*=1$ ($1/\Gamma_M\approx 0.060$) is one order of magnitude smaller than that for $m^*=s_B$ ($1/\Gamma_M\approx 0.138$). This is another example of how the composition changes drastically the properties of the system.

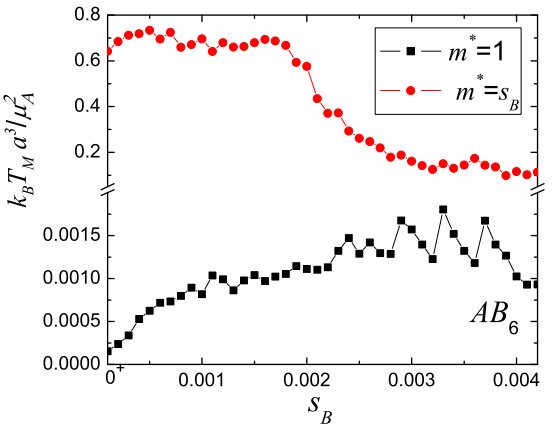

FIG. 13. (Color online) Melting temperature of the A sublattice for the structure AB_6 as a function of the dipole-moment ratio. $m^*=1$ ($m^*=s_B$) means particles A and B with equal (different) masses. The melting temperature for $m^*=1$ reaches its maximum value when $s_B=0.0033$.

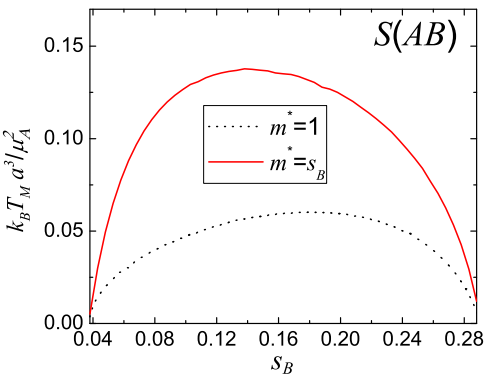

FIG. 14. (Color online) Melting temperature of the A sublattice for the configuration $S(AB)$ as a function of the dipole-moment ratio. Here, for $m^*=1$, the maximum temperature $1/\Gamma_M\approx 0.060$ takes place for $s_B=0.18$, while for $m^*=s_B$, the maximum temperature $1/\Gamma_M\approx 0.138$ occurs for $s_B=0.138$.

V. CONCLUSIONS

We investigated the dynamical properties and melting transition of a 2D binary colloidal system of dipoles interacting through a dipole-dipole repulsive potential. Within the *harmonic approximation* we calculated the phonon spectra of the system as a function of the relative concentration of small particles, dipole-moment ratio, and mass ratio. We determined the interval of values of the dipole-moment ratio s_B for which the colloidal alloys with perfect hexagonal arrangement are stable and have long-range order. For instance, we found that the AB_2 configuration has long-range order for $s_B \lesssim 0.0269$.

For the phase AB_5 we found that the $T = 0$ phonon spectrum consists of imaginary frequencies, indicating that the perfect hexagonal AB_5 structure is unstable. We did not find a long-range AB_6 ordered configuration for $s_B = 0.037$ which is consistent with the experiments reported in Ref. [15].

The gaps in the phonon spectra were analyzed by changing the composition, mass ratio, and the dipole-moment ratio. For example, the phonon gaps of the configurations AB_2 and AB_6 are considerably large when the particles have different masses. Furthermore, unlike the colloidal alloys AB_2 and AB_6 that have phonon gaps when the particles have different masses as well as equal masses, the configuration $S(AB)$ exhibits phonon gaps only when the particles have different masses. This is an example of how the composition changes the properties of the system. The optical frequencies in the long-wavelength limit were discussed. The number of optical frequencies is associated with the number of particles per unit cell, i.e., the composition. The optical frequencies of the phase $S(AB)$ are degenerate while the ones of the configurations AB_2 and AB_6 are not. The common behavior that the optical frequencies go to zero when the dipole-moment ratio tends to zero does not hold when particles have different masses ($m^* = s_B$). We also analyzed the sound velocity of the transverse acoustical mode. As a general behavior, the sound velocity becomes large when the particles have different masses. Furthermore, the speed of sound depends strongly on the composition and the dipole-moment ratio. For instance, for the composition $\xi = 6/7$ (AB_6) the sound velocity along the ΓX direction diminishes only until $s_B = 0.00251$, where the minimum speed of sound is obtained.

We estimated the melting temperature of the A sublattice as a function of the dipole-moment ratio and composition, within the harmonic approximation, and using the modified Lindemann criterion. For each stable configuration, we determined the value of the dipole-moment ratio for which the melting temperature is a maximum. This is also an important result that will be useful in future experiments of 2D binary colloidal systems of dipoles.

ACKNOWLEDGMENTS

This work was supported by the Brazilian agencies CNPq (Program Science Without Border), CAPES, and FUNCAP (International cooperation program); the Flemish Science Foundation (FWO-Vl); the bilateral program between Flanders and Brazil (CNPq-FWO collaborating project); and the VLIR-UOS (University Development Cooperation). I.R.O.R. is grateful to Professor E. B. Barros for fruitful discussions. W.P.F. thanks Professor D. Martin A. Buzza for his illuminating comments on this manuscript.

[1] U. Gasser, C. Eisenmann, G. Maret, and P. Keim, Chem. Phys. Chem. **11**, 963 (2010).
[2] K. Zahn, R. Lenke, and G. Maret, Phys. Rev. Lett. **82**, 2721 (1999).
[3] F. Ebert, P. Dillmann, G. Maret, and P. Keim, Rev. Sci. Instrum. **80**, 083902 (2009).
[4] P. Schall, I. Cohen, D. A. Weitz, and F. Spaepen, Nature (London) **440**, 319 (2006).
[5] A. M. Alsayed, M. F. Islam, J. Zhang, P. J. Collings, and A. G. Yodh, Science **309**, 1207 (2005).
[6] P. Keim, G. Maret, U. Herz, and H. H. von Grünberg, Phys. Rev. Lett. **92**, 215504 (2004).
[7] Sofi Nöjd, Priti S. Mohanty, Payam Baheri, Anand Yethiraj, and Peter Schurtenberger, Soft Matter **9**, 9199 (2013).
[8] T. Stirner and J. Sun, Langmuir **21**, 6636 (2005).
[9] L. Assoud, R. Messina, and H. Löwen, Europhys. Lett. **80**, 48001 (2007).
[10] Julia Fornleitner, Federica Lo Verso, Gerhard Kahl, and Christos N. Likos, Soft Matter **4**, 480 (2008).
[11] J. Fornleitner, F. Lo Verso, G. Kahl, and C. N. Likos, Langmuir **25**, 7836 (2009).
[12] N. Hoffmann, C. Likos, and H. Löwen, J. Phys.: Condens. Matter **18**, 10193 (2006).
[13] N. Hoffmann, F. Ebert, C. N. Likos, H. Löwen, and G. Maret, Phys. Rev. Lett. **97**, 078301 (2006).
[14] F. Ebert, P. Keim, and G. Maret, Eur. Phys. J. E **26**, 161 (2008).
[15] A. D. Law, D. M. A. Buzza, and T. S. Horozov, Phys. Rev. Lett. **106**, 128302 (2011).
[16] A. D. Law, T. S. Horozov, and D. M. A. Buzza, Soft Matter **7**, 8923 (2011).
[17] J. Fornleitner, G. Kahl, and C. N. Likos, Phys. Rev. E **81**, 060401(R) (2010).
[18] L. Bonsall and A. A. Maradudin, Phys. Rev. B **15**, 1959 (1977).
[19] G. Goldoni and F. M. Peeters, Phys. Rev. B **53**, 4591 (1996).
[20] Xin Lu, Chang-Qin Wu, Andrea Micheli, and Guido Pupillo, Phys. Rev. B **78**, 024108 (2008).
[21] I. R. O. Ramos, W. P. Ferreira, F. F. Munarin, G. A. Farias, and F. M. Peeters, Phys. Rev. E **85**, 051404 (2012).
[22] G. P. Srivastava, *The Physics of Phonons* (Adam Hilger, Bristol, 1990).
[23] A. A. Maradudin, E. W. Montroll, G. H. Weiss, and I. P. Ipatova, *Theory of Lattice Dynamics in the Harmonic Approximation* (Academic Press, New York, 1971), Suppl. 3.
[24] H. H. von Grünberg and J. Baumgartl, Phys. Rev. E **75**, 051406 (2007).

[25] N. Osterman, D. Babic, I. Poberaj, J. Dobnikar, and P. Ziherl, Phys. Rev. Lett. **99**, 248301 (2007).
[26] F. A. Lindemann, Physik. Z. **11**, 609 (1910).
[27] D. Pines, *Elementary Excitations in Solids* (W. A. Benjamin, New York, 1963).
[28] V. M. Bedanov, G. V. Gadiyak, and Y. E. Lozovik, Phys. Lett. A **109**, 289 (1985).
[29] W. P. Ferreira, G. A. Farias, and F. M. Peeters, J. Phys.: Condens. Matter **22**, 285103 (2010).
[30] K. Zahn and G. Maret, Phys. Rev. Lett. **85**, 3656 (2000).